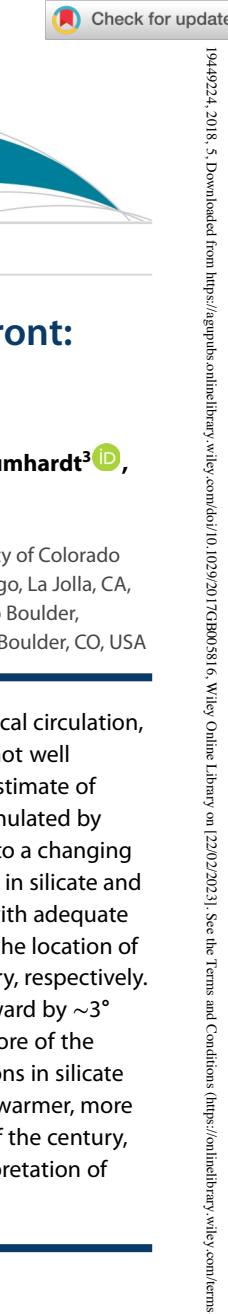
-and-conditions) on Wiley Online Library for rules of use; OA articles are governed by the applicable Creative Commons License





# **Global Biogeochemical Cycles**

## RESEARCH ARTICLE

10.1029/2017GB005816

#### **Key Points:**

- · Silicate Front position is influenced by biology and bathymetry on seasonal to interdecadal time scales
- Twenty-first century climate warming drives a poleward shift in the Silicate Front independent of the Antarctic
- A more poleward Silicate Front is driven by a combination of increased stratification and silicate utilization

#### **Supporting Information:**

• Supporting Information S1

#### **Correspondence to:**

N. M. Freeman, n2freeman@ucsd.edu

#### Citation:

Freeman, N. M., Lovenduski, N. S., Munro, D. R., Krumhardt, K. M., Lindsay, K., Long, M. C., & Maclennan, M. (2018). The variable and changing Southern Ocean Silicate Front: Insights from the CESM Large Ensemble. Global Biogeochemical Cycles, 32, 752-768. https://doi.org/10.1029/2017GB005816

Received 12 OCT 2017 Accepted 3 APR 2018 Accepted article online 10 APR 2018 Published online 8 MAY 2018

## The Variable and Changing Southern Ocean Silicate Front: **Insights From the CESM Large Ensemble**

Natalie M. Freeman<sup>1,2</sup>, Nicole S. Lovenduski<sup>1</sup>, David R. Munro<sup>1</sup>, Kristen M. Krumhardt<sup>3</sup> Keith Lindsay<sup>4</sup>, Matthew C. Long<sup>4</sup>, and Michelle Maclennan<sup>1</sup>

<sup>1</sup>Department of Atmospheric and Oceanic Sciences and Institute of Arctic and Alpine Research, University of Colorado Boulder, Boulder, CO, USA, <sup>2</sup>Now at Scripps Institution of Oceanography, University of California, San Diego, La Jolla, CA, USA, <sup>3</sup> Environmental Studies Program and Institute of Arctic and Alpine Research, University of Colorado Boulder, Boulder, CO, USA, <sup>4</sup>Climate and Global Dynamics Laboratory, National Center for Atmospheric Research, Boulder, CO, USA

**Abstract** The location of the Southern Ocean Silicate Front (SF) is a key indicator of physical circulation, biological productivity, and biogeography, but its variability in space and time is currently not well understood due to a lack of time-varying nutrient observations. This study provides a first estimate of the spatiotemporal variability of the SF, defined using the silicate-to-nitrate (Si:N) ratio as simulated by the Community Earth System Model (CESM) Large Ensemble (1920 – 2100), and its response to a changing Southern Ocean. The latitude where Si:N = 1 largely coincides with regions of high gradients in silicate and the observed position of the Antarctic Polar Front (PF) and serves as an indicator of waters with adequate nutrients available for diatom growth. On seasonal to interdecadal time scales, variability in the location of the SF is largely determined by biological nutrient utilization and Southern Ocean bathymetry, respectively. From 1920 to 2100, under historical and RCP8.5 forcing, the zonally averaged SF shifts poleward by  $\sim$ 3° latitude, with no discernible shift in the position of the simulated location of the PF or the core of the Antarctic Circumpolar Current. A more poleward SF is primarily driven by long-term reductions in silicate and nitrate concentrations at the surface as a consequence of greater iron availability and a warmer, more stratified Southern Ocean. These results suggest a decoupling of the SF and PF by the end of the century, with implications for local biogeography, global thermocline nutrient cycling, and the interpretation of paleoclimate records from deep sea sediments.

## 1. Introduction

The Antarctic Circumpolar Current (ACC) system of the Southern Ocean is made up of many dynamically and biogeochemically distinct regions due to the presence of hydrographic fronts and geostrophic jets (Belkin & Gordon, 1996; Deacon, 1937, 1982; Dong et al., 2006; Freeman et al., 2016; Moore et al., 1999; Orsi et al., 1995; Pollard et al., 2002; Sokolov & Rintoul, 2009b, 2009a). ACC fronts are characterized by strong lateral property gradients (e.g., temperature and salinity) associated with sloping density surfaces. Fronts of biogeochemically important properties often coincide with ACC fronts and jets. Biogeochemical frontal zones are sites where mixing and advection supply nutrients to the euphotic zone, directly influencing local primary production; indeed, enhanced phytoplankton biomass and elevated concentrations of satellite-derived chlorophyll a and calcite are found to be coincident with ACC fronts (Balch et al., 2016; Moore & Abbott, 2000; Smetacek et al., 1997), particularly at bathymetric features (Sokolov & Rintoul, 2007). While the Southern Ocean is characterized as a high-nutrient, low-chlorophyll region, ACC fronts mark locations where nutrients return from depth before feeding the low-latitude thermocline (Marinov et al., 2006; Palter et al., 2010; Sarmiento et al., 2004).

The Antarctic Polar Front (PF) is one of the major hydrographic fronts of the ACC known for its signature sharp meridional gradient in temperature, reflecting both subduction and transition zones: here cold, fresh Antarctic surface waters subduct beneath warmer, saltier subantarctic waters and from south to north across the PF, stratification transitions from a salinity-dominated regime to a temperature-dominated regime (Pollard et al., 2002). Biogeochemically, the PF marks the boundary between silicate-rich and silicate-poor waters (Pollard et al., 2002; Sarmiento et al., 2004). This distinction is important to diatoms, which are the dominant phytoplankton taxa in the Southern Ocean and require silicic acid (Si) to produce and maintain their silica

©2018. American Geophysical Union. All Rights Reserved.

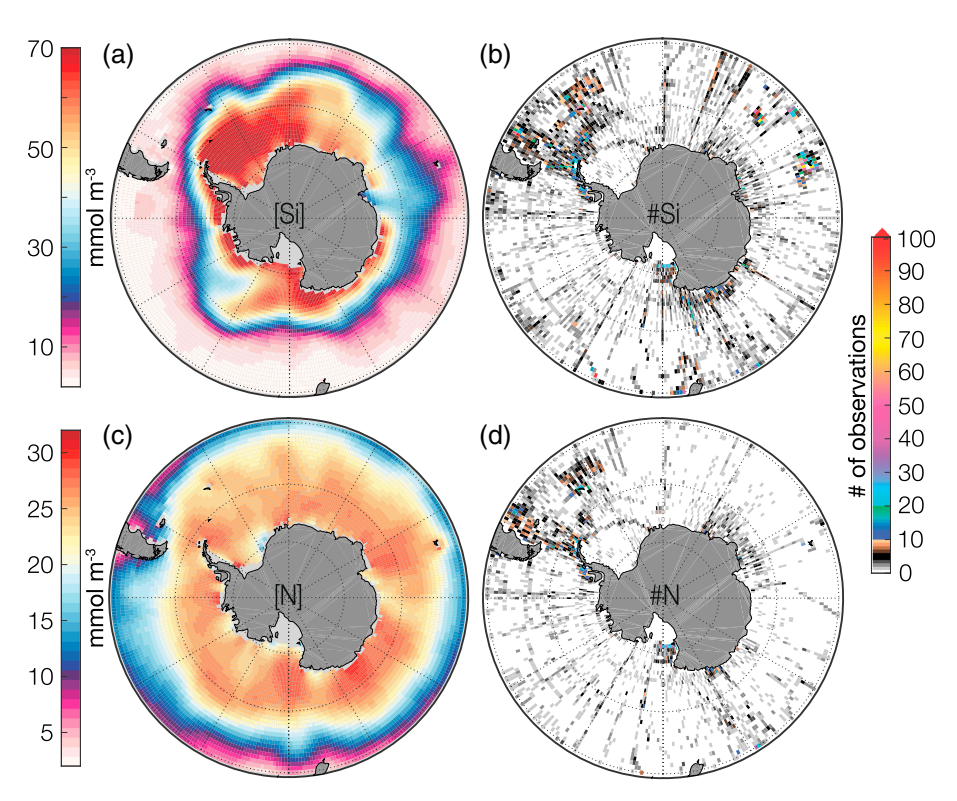


**Figure 1.** Climatological annual mean surface (a) silicate and (c) nitrate concentration and the number of available observations of (b) silicate and (d) nitrate in each  $1^{\circ} \times 1^{\circ}$  surface grid cell. Data from the World Ocean Atlas 2013 (Boyer et al., 2013).

frustules. The westerly winds drive the upwelling and mixing of Si-rich Upper Circumpolar Deep Water south of the PF, and as Upper Circumpolar Deep Water travels northward across the frontal zone through Ekman transport, diatoms strip the available Si (e.g., Franck et al., 2000; Leynaert et al., 2004), setting up the Southern Ocean Silicate Front (SF). The PF/SF is therefore regarded as an important boundary for the biogeography of the Southern Ocean (i.e., the geographic distribution of diatoms versus nonsiliceous phytoplankton). Surface properties set at these frontal zones ultimately have an impact on global nutrient cycling: these Si-poor waters are subsequently exported to the low-latitude thermocline through the subduction of mode and intermediate waters northward (see Sarmiento et al., 2004; Tréquer, 2014).

In addition to its important role in the global carbon cycle (e.g., Munro, Lovenduski, Takahashi et al., 2015), the Southern Ocean is also a region of large Si flux from the surface to deep ocean (DeMaster, 2002; Pondaven et al., 2000; Tréguer et al., 1995). The Si-rich waters south of the PF support high diatom abundance and biogenic silica (i.e., opal) production. The resulting high export production out of the surface and, ultimately, the burial of opal in abyssal sediments contribute to the Southern Ocean Opal Belt of siliceous sediments that ring the Antarctic, roughly mirroring the surface PF zone (DeMaster, 1981, 2002). The relationship between the locations of the PF/SF and the Opal Belt has been instrumental in reconstructing past climates (see section 4.1.3; e.g., Kemp et al., 2010).

Previous studies have considered the spatial and temporal variability in the position of the Southern Ocean PF, but the variability in the associated SF is not well understood due to limited observations (Figure 1). Quantifying and understanding the spatiotemporal variability of the SF and, in particular, changes in the SF driven by anthropogenic climate change, provides insight into controls on Southern Ocean biogeography, interpretation of sedimentary opal records, and export of nutrients to low latitudes on various time scales. In this study, we identify the Southern Ocean SF in an ensemble of a state-of-the-art coupled climate model, track its variability in space and time, and quantify its long-term change under a high-emission scenario.

## 2. Methods

#### 2.1. Front Definition

In this study, we define the position of the Southern Ocean SF as the latitude poleward of  $44^{\circ}$ S where Si: N = 1. We choose Si: N = 1 as a marker of the SF for the following reasons:

- 1. The latitude where Si:N = 1 exhibits high correspondence between high absolute gradients in simulated Si and the observed PF (not shown) and thus can be used to track the location of the SF without tracking individual gradients.
- 2. This ratio has been formerly invoked (as  $Si^* = Si N = 0$  in Sarmiento et al., 2004) to track macronutrient availability and water mass formation.
- 3. This ratio simultaneously tracks Si and N, which are both important for phytoplankton growth.
- 4. Si:N = 1 has biological significance. Under sufficient light and nutrient conditions, the Si demand of most diatoms is equivalent to that for nitrate (N); that is, a Si:N depletion ratio of 1 (Ragueneau et al., 2000; Smetacek, 1999). North of the Si:N = 1 latitude, diatoms are more likely to experience Si limitation (Nelson et al., 2001).

In the analyses that follow, we define the absolute gradient in a given variable V as

$$|\nabla V| = \sqrt{(\delta V/\delta x)^2 + (\delta V/\delta y)^2},$$

where  $\delta V$  is the unit difference in the variable and  $\delta x$  and  $\delta y$  are the kilometer distances between any two longitude or latitude points, respectively. As in Freeman and Lovenduski (2016), we refer to the gradient identified at a front as the intensity or strength of that front (e.g., the absolute Si gradient at the SF,  $|\nabla Si|$ , is an indication of the strength of the SF).

#### 2.2. Observations

Objectively analyzed climatological annual mean surface Si and N concentrations taken from the World Ocean Atlas 2013 (WOA13; Boyer et al., 2013; Garcia et al., 2013) are shown in Figures 1a and 1c. These climatologies represent an average of all nutrient data collected since the mid-1900s, interpolated to standard depth levels (here surface refers to standard depth level 1) on a 1° grid. Figures 1b and 1d highlight the historic undersampling of the Southern Ocean with respect to Si and N, with the majority of locations having only a single surface observation over the last century. Figures 1b and 1d also demonstrate a higher data density for Si than N in most Southern Ocean locations.

Here we take advantage of an independent macronutrient data set not included in the WOA13, collected as part of the ongoing Drake Passage Time-series (DPT) program. Discrete surface samples of Si and N were collected on five to eight transects of the Drake Passage per year from 2005 to 2016 at approximately every half-degree of latitude from the Antarctic Research Supply Vessel *Laurence M. Gould*, representing a high data density across the ACC not represented by the WOA13; a description of macronutrient sampling methods used by the DPT can be found in Munro, Lovenduski, Stephens et al. (2015).

# 2.3. Community Earth System Model Large Ensemble 2.3.1. Model Description

We investigate intra-annual to interdecadal variability and long-term change in the Southern Ocean SF using monthly output from the Community Earth System Model Large Ensemble (CESM-LE) simulations (described in detail in Kay et al., 2015). In short, CESM version 1 (CESM1) is a state-of-the-art coupled climate model run with atmosphere, ocean (nominal 1° horizontal resolution and 60 vertical levels), land, and sea ice components (Danabasoglu et al., 2012; Hunke & Lipscomb, 2008; Hurrell et al., 2013; Smith et al., 2010). The ocean biogeochemical component has three explicit phytoplankton functional types (PFTs; Moore et al., 2004, 2013), a dynamic iron cycle (Doney et al., 2006; Moore & Bracuher, 2008), and full carbonate system thermodynamics and allows for multinutrient colimitation. The three PFTs represented in the model include small phytoplankton, diatoms, and diazotrophs (Moore et al., 2004, 2013); as this study focuses solely on the Southern Ocean, our investigation is limited to small phytoplankton and diatom PFTs. Each PFT has a maximum growth rate that is scaled directly by a temperature function (with a Q10 of 2.0 and a reference temperature of 30°C) and is further attenuated by light and nutrient limitation. Zooplankton grazing can also affect these PFTs, with grazing rates increasing with temperature. In general, given the prescribed model parameterizations, diatoms are more productive in cooler, high-nutrient conditions (e.g., south of the PF and SF), while small phytoplankton

are more productive in warmer, low-nutrient conditions (owing to smaller half-saturation constants for nutrient uptake) and experience higher grazing pressure than diatoms.

The CESM-LE included a control integration (>2,000 years) and 34 ensemble members with ocean biogeochemistry output (Kay et al., 2015; Lovenduski et al., 2016). A great advantage to using a large ensemble of a single Earth System Model (ESM) is the ability to isolate and investigate internal (i.e., natural) climate variability without the effects of model structural uncertainty (e.g., when using the CMIP5 model simulations; see Lovenduski et al., 2016). Atmospheric  $CO_2$  concentrations are prescribed in the CESM-LE, and all ensemble members have identical external forcing: historical forcing from 1920 to 2005 and RCP8.5 forcing from 2006 to 2100. Beginning from an 1850 control simulation with constant preindustrial forcing, the first ensemble member (EM001) was initialized from a randomly selected year (402) of the control and integrated forward in time to 2100. The remaining ensemble members were then integrated from 1920 to 2100 using initial conditions from EM001 at 1920 but with added minute ( $\mathcal{O}(10^{-14})$  K) perturbations in initial air temperature; since each ensemble member simulation is identically forced, such perturbations result in different natural (internal) climate variability across members. Therefore, the ensemble mean of any simulated variable is a representation of the long-term forced trend, while variance across members can be attributed to the influence of internal climate variability on that variable (McKinley et al., 2016, 2017).

## 2.3.2. Statistical Analysis of Model Output

For a given month and desired depth level, ensemble mean values of simulated variables were computed by averaging across ensemble members. Decadal averages of simulated variables were computed for historical conditions (1920–1929; referred to as 1920s), present-day conditions (2000–2009; referred to as 2000s), and future conditions (2090–2099; referred to as 2090s) for each ensemble member and for the ensemble mean. Here we report long-term change in the ensemble mean as an epoch difference between the present-day and future mean (2090s – 2000s) and use variation across the ensemble members to evaluate where change is robust: statistical significance of long-term change is defined as any location where the ensemble mean epoch difference exceeds one standard deviation of the differences across ensemble members (i.e., where the signal-to-noise ratio, the ratio of ensemble mean change over interensemble standard deviation, exceeds 1). We define sea ice extent as the northernmost grid point where simulated sea ice fraction exceeds 0.1; the presence of sea ice in winter can sometimes preclude the detection of the SF.

## 2.3.3. Model Evaluation

The biogeochemical (Biogeochemical Elemental Cycling [BEC]; Moore et al., 2004, 2013) and physical ocean (Parallel Ocean Program, version 2 [POP2]; Danabasoglu et al., 2012; Smith et al., 2010) models used in the CESM-LE have been evaluated in previous studies. Misumi et al. (2014) find a skillful reproduction of the known high-nutrient, low-chlorophyll regions (e.g., the iron-limited Southern Ocean) as compared to the field observations of Tagliabue et al. (2012), and Tagliabue et al. (2016) find the BEC model to closely match interior ocean observations of Fe\*, the relative inventories of iron (Fe) and N, in the Atlantic basin. Moore et al. (2013) document model skill in simulating observed ecology: surface nutrient, phytoplankton biomass, temperature, and salinity distributions compare favorably with observations (see also Bates et al., 2012; Danabasoglu et al., 2012; Long et al., 2013), while other biogeochemical metrics are also captured, such as large-scale air-sea CO<sub>2</sub> flux (Long et al., 2013; Lovenduski et al., 2016; McKinley et al., 2016) and net primary productivity (Krumhardt et al., 2017) patterns compared to observational climatologies and satellite-based estimates, respectively. Farneti et al. (2015) determine the ocean component to be one of the more realistic climate models in terms of model physics, largely owing to its three-dimensional time-varying specification of the Gent-McWilliams (GM) coefficient (Gent et al., 1995; Gent & McWilliams, 1990), a skillful parameterization of mesoscale eddies. Danabasoglu et al. (2012) document the model's success in reproducing Drake Passage transport, as compared to the observational estimates of Cunningham et al. (2003) and, more recently, Donohue et al. (2016). Therefore, the CESM-LE is suitable for investigating variability and change in the Southern Ocean SF and its associated physical and biogeochemical processes in the context of climatic change.

We validate the modeled surface ocean Si concentration and the modeled position of the SF using data from the DPT (see section 2.2). Figure 2 compares the mean surface Si concentration as observed (DPT, colored circles) and simulated (CESM-LE, colored map) across the Drake Passage from 2005 to 2016. To account for the spatial distribution in ship crossings, DPT macronutrients were averaged zonally at an orientation roughly parallel to the mean flow of the ACC and gridded onto the most commonly followed cruise track across Drake Passage (colored circles in Figure 2; gridding similar to Munro, Lovenduski, Stephens et al., 2015). The CESM-LE underestimates Si in the southern Drake Passage and overestimates Si in the northern Drake Passage.

19449224, 2018, 5, Downloaded from https://agupubs.onlinelibrary.wiley.com/doi/10.1029/2017GB005816, Wiley Online Library on [22/02/2023]. See the Terms and Conditions (https://onlinelibrary.wiley.com/terms

and-conditions) on Wiley Online Library for rules of use; OA articles are governed by the applicable Creative Commons Licenso

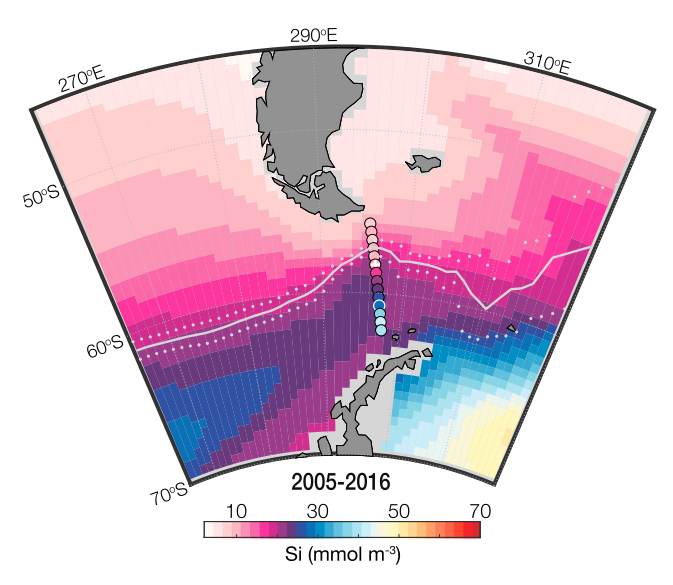


**Figure 2.** Mean surface Si concentration (color) within the Drake Passage region as represented by the Community Earth System Model Large Ensemble mean (map) and from the Drake Passage Time-series (DPT; filled circles) over 2005–2016. DPT Si follows a mean transect line representing the majority of Drake Passage crossings (see section 2.3.3). Along this DPT main line, the white plus sign marks the location where the DPT data indicate a sharp meridional gradient in Si (the observed Silicate Front) and the white open circle marks the location where Si:N = 1 in the DPT data. Community Earth System Model Large Ensemble mean (gray contour) and standard deviation ( $\pm 1\sigma$ ; gray dots) in the Silicate Front position (2005–2016).

The largest meridional gradient in observed Si (white plus sign, Si:N  $\approx$  0.5) falls just outside the modeled range in SF position (gray contour and bounding dots). The observations suggest that the latitude where Si:N = 1 (white open circle) is located south of the modeled SF. We attribute this to the known nutrient biases in the model (see Moore et al., 2013).

#### 2.4. CMIP5 Models

To provide context for the CESM-LE results, we examine the present-day (2000s; decadal average over 2000–2009) surface mean Si concentration from a subset of the Coupled Model Intercomparison Project, phase 5 (CMIP5; Taylor et al., 2012) models: the MPI-ESM-LR from the Max Planck Institute (MPI; Giorgetta et al., 2013; Ilyina et al., 2013), GFDL-ESM2M from the Geophysical Fluid Dynamics Laboratory (GFDL; Dunne et al., 2012, 2013), and HadGEM2-ES from the UK Met Office Hadley Centre (Collins et al., 2011; HadGEM2 Development Team, 2011; Palmer & Totterdell, 2001). Just as in the CESM-LE, historical forcing was applied through 2005, followed by RCP8.5 forcing through 2100. The CESM-LE is most suited for investigating the mean state and variability of the Southern Ocean SF, as the remaining CMIP5 ESMs analyzed here exhibit a high Si bias throughout the Southern Ocean (supporting information Figures S1c–S1e), resulting in a misrepresentation of the location and properties of the SF that largely disagree with observations (Figure S1a; see also, e.g., Palter et al., 2010; Smith Jr. et al., 2000).

#### 3. Results

#### 3.1. Mean State

Figures 3a and 3b display the CESM-LE present-day ensemble mean Southern Ocean surface Si and N concentration, respectively. In general, from north to south, Si and N concentrations increase toward the Antarctic continent, consistent with observations (Figures 1a and 1c). The large-scale biogeochemical fronts of Si and N that have historically characterized the Southern Ocean are captured by the CESM-LE, marked by a sharp meridional gradient in each nutrient, with the SF generally found to the south of the Nitrate Front (Figures 3a and 3b; compare to Figures 1a and 1c; see Palter et al., 2013; Sarmiento et al., 2004).

Figure 3c shows the CESM-LE present-day ensemble mean expressions of the SF at the surface (black solid contour) and at 200 m depth (black dashed contour) overlain on the ensemble mean Si:N ratio in the surface layer. The climatological ensemble mean path of the surface SF is zonally asymmetric, traversing  $\sim 12^{\circ}$  of latitude from its northernmost position along the Mid-Atlantic Ridge (49.41°S) to its southernmost position

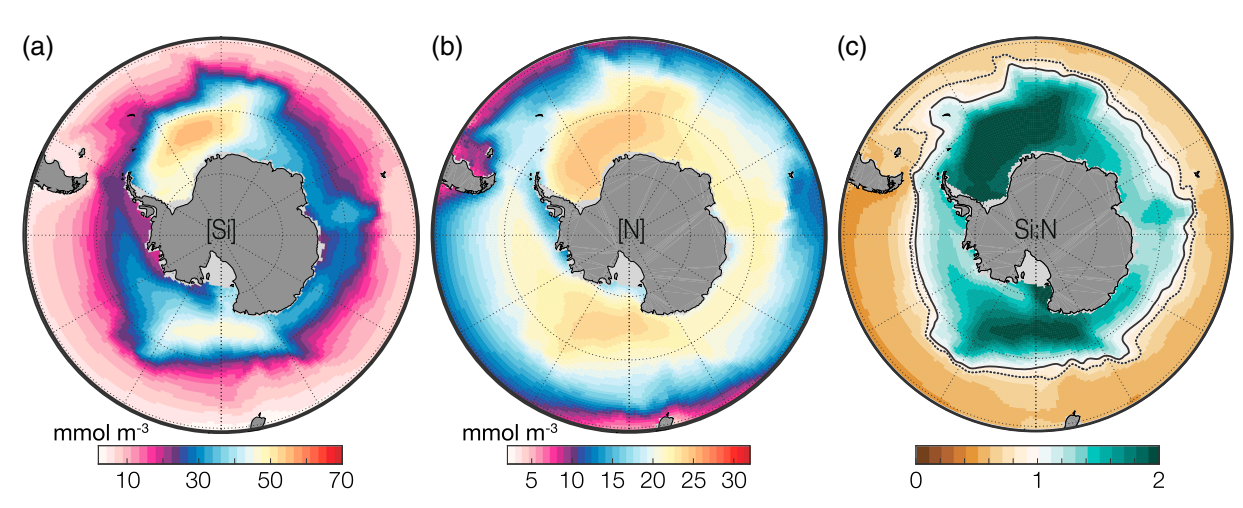


Figure 3. Community Earth System Model Large Ensemble simulated present-day (2000s; decadal average over 2000–2009) ensemble mean (a) Si and (b) N concentration and (c) their ratio, Si:N, at the surface (colors). Black contours in (c) indicate the latitude where Si:N = 1 at the surface (solid) and at 200 m (dashed).

in the southeast Pacific (61.47°S; Figure 3c). The climatological Si concentration (and the N concentration, by definition) at the SF ranges from 16.27 to 21.14 mmol/m³. The climatological intensity ( $|\nabla Si|$ ; see section 2) of the surface SF ranges from 1.03 mmol/m³ per 100 km southwest of Kerguelen, a region characterized by deep bathymetry, to 8.57 mmol/m³ per 100 km across the Pacific-Antarctic Ridge, a region characterized by shallow bathymetry; averaged over all longitudes, SF intensity is ~2.91 mmol/m³ per 100 km.

This persistent, large-scale nutrient front has a near-surface expression, characterized by property gradients that can extend below 200 m (see Palter et al., 2013). Figure 3c highlights that the subsurface expression of the SF, located at 200 m depth, is consistently found to the north of the surface expression, with largest latitudinal differences between the surface and subsurface fronts found in the Scotia Sea sector and smallest differences found in regions characterized by shallow bottom depths (Figure 3c). Indeed, Si is found to be enriched at depth (consistent with WOA13; not shown) relative to N (high Si:N ratio at depth), reflecting the vertical segregation of organic matter remineralization and opal dissolution (as suggested by Broecker & Peng, 1982). While spatial variability in the surface SF can be driven by surface processes (e.g., biological nutrient utilization and air-sea fluxes), variability in the surface and subsurface expression are tightly linked and our analyses of both expressions of the SF reveal similar results. Therefore, in the following subsections, we choose to report variability and long-term change in the surface expression of the SF.

## 3.2. Seasonal Variability

We find that the present-day CESM-LE zonal mean position and intensity of the surface SF and its associated Si concentration exhibits a clear seasonal cycle (Figure 4). The SF resides in its most northerly position in January and September and its most southerly position during austral autumn (March-April-May; Figure 4a). In late summer to early autumn, the SF contracts poleward, reflecting the seasonal drawdown of Si by diatoms to the south of the SF and the relative preference for N over Si north of the SF, followed by an expansion northward during the winter months (June-July-August), reflecting a return supply of Si from below and a lack of consumption by phytoplankton. It follows that the Si concentrations found at the SF are largest in late winter to early spring and smallest in late summer to early winter (Figure 4b). During this poleward contraction, first, the SF intensifies, characterized by its strongest gradients in February, closely followed by a weakening, characterized by its weakest gradients in April (Figure 4c). In general, the mixed layer depth (MLD) at the zonal mean SF shoals in early to mid summer and deepens from February to September, while the sea surface temperature (SST) characterizing the SF is warmest in summer and coolest throughout the late winter to early spring months (not shown).

Regionally, the amplitude of the seasonal cycle in the position of the SF can exceed that of the zonal average ( $\sim$ 1° latitude; Figure 4a) by several degrees of latitude, consistent with in situ studies such as Smith Jr. et al. (2000). Near major topographic features, the amplitude of the seasonal cycle tends to change over time (i.e., is nonstationary), highlighting the influence of topography on the position of the SF; for example,

19449224, 2018. 5, Downloaded from https://agupubs.onlinelibrary.wiley.com/doi/10.1029/2017GB005816, Wiley Online Library on [22/02/2031]. See the Terms and Conditions (https://onlinelibrary.wiley.com/terms-and-conditions) on Wiley Online Library for rules of use; OA articles are governed by the applicable Creative Commons Licenses

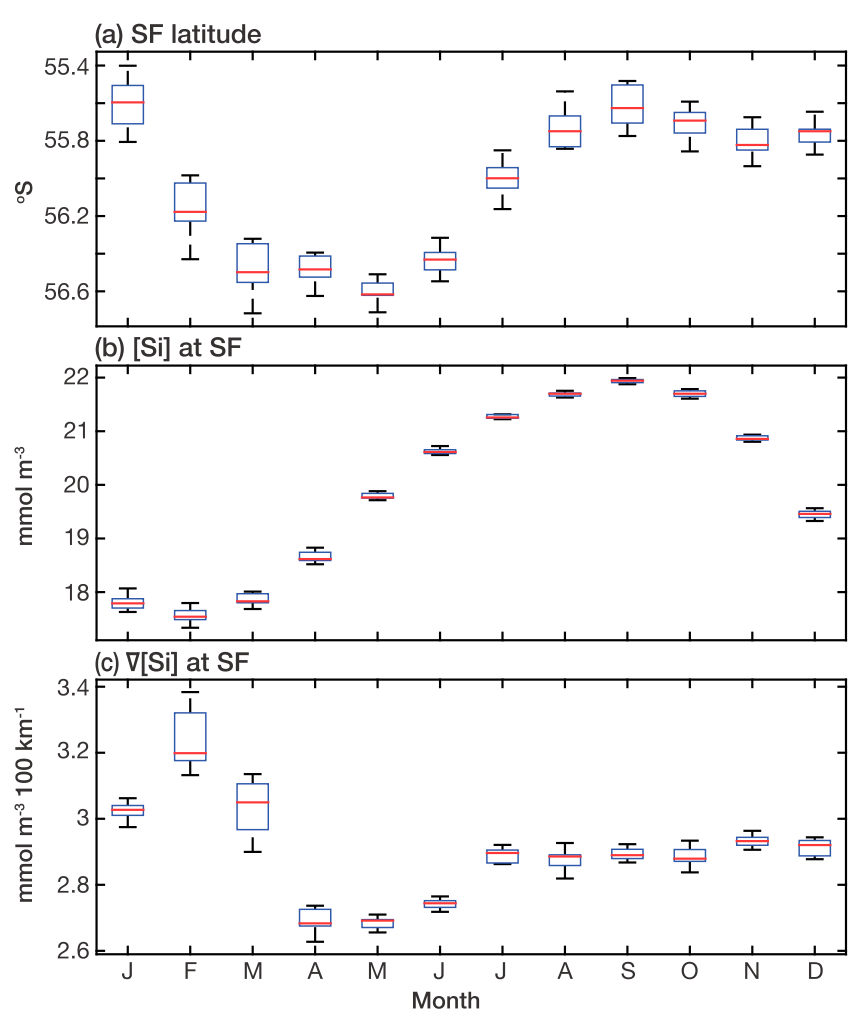


**Figure 4.** From 2000 to 2009, Community Earth System Model Large Ensemble mean zonally averaged (a) Silicate Front (SF) latitude, (b) Si concentration at the SF, and (c) intensity of the SF, by month (sample size n = 10 for each month); each box and whisker indicates the median value (center red line), 25th and 75th percentiles (blue horizontal edges; interquartile range), and extreme data points not considered outliers (black whiskers; standard Tukey style; see Krzywinski & Altman, 2014).

on the leeward side of the Mid-Atlantic Ridge, both the windward and leeward side of Kerguelen Plateau, and leeward of the Pacific-Antarctic Ridge, the north-south extent of the SF is greater in future relative to present day (not shown).

## 3.3. Interannual to Interdecadal Variability

We find that interannual to interdecadal variability in the position of the CESM-LE SF is influenced by the underlying bathymetry, with greatest variability over deep-ocean depths. Congruently, Freeman et al. (2016) show that from 2002 to 2014, the standard deviation in the monthly PF varies from 0.19° over shallow bathymetry to 2.0° over deep bathymetry. In comparison to the observed PF, the standard deviation in the present-day monthly CESM-LE SF can be as low as 0.05° near Kerguelen Plateau and as large as 1.75° over the deeper Indian sector. One exception is the  $\sim 300-330^\circ$ E sector, where interannual variability can be as large as  $\sim 4^\circ$  latitude, owing to high variability in the background Si concentration rather than the underlying bathymetry.

In the deep ocean where variability is greatest, interannual variance in the position of the SF grows over the 21st century (i.e., is nonstationary). For example, in the southeast Indian sector ( $\sim$ 100°E), the standard deviation in the monthly SF position is consistently  $\sim$ 1° latitude during the 20th century but nears  $\sim$ 3° latitude throughout the 21st.

19449224, 2018, 5, Downloaded from https://agupubs.onlinelibrary.wiley.com/doi/10.1029/2017GB005816, Wiley Online Library on [2202/2023]. See the Terms and Conditions (https://onlinelibrary.wiley.com/rerms

-and-conditions) on Wiley Online Library for rules of use; OA articles are governed by the applicable Creative Commons Licenso

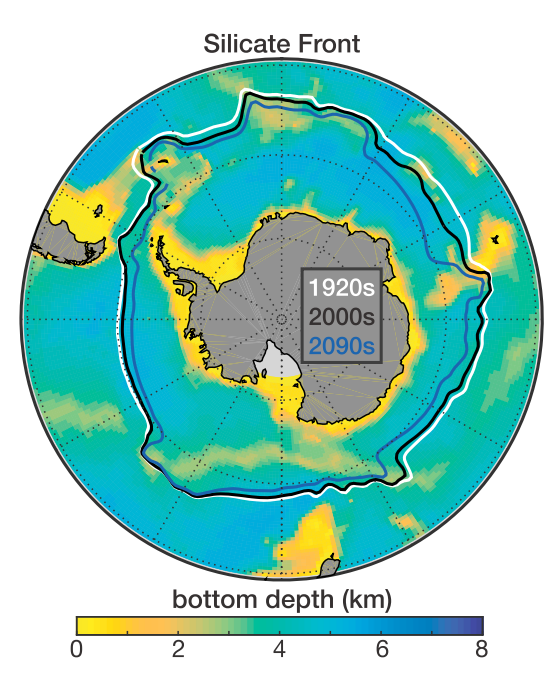


**Figure 5.** Decadal mean Silicate Front positions: historical (1920s; white contour), present-day (2000s; black contour), and future (2090s; blue contour) mean location. Bathymetry, or bottom depth, as simulated by the Community Earth System Model version 1, displayed underneath Silicate Front positions in color, where warm colors indicate shallow bathymetry and cool colors indicate deep.

Figure 5 displays the historical, present, and future decadal mean SF positions overlain on CESM1 bathymetry. We find that interdecadal variability of the SF is influenced by this underlying bathymetry, an influence similar to the interannual variability reported for the PF over the shorter observational record (Chelton et al., 1990; Deacon, 1937; Dong et al., 2006; Freeman et al., 2016; Gille, 1994; Gordon et al., 1978; Moore et al., 1999; Sallée et al., 2008). Interdecadal variability of the SF is low along the Mid-Atlantic and Pacific-Antarctic ridges and across the Kerguelen Plateau, and larger over the deeper basins, particularly in the  $\sim 30-70^{\circ}$ E sector.

## 3.4. Long-Term Change

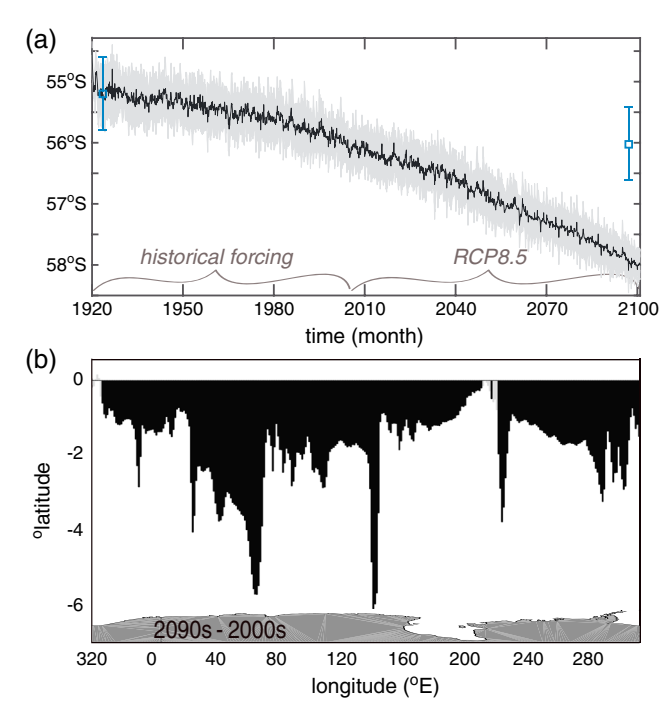
From 1920 to 2100, we find that the monthly, zonally averaged ensemble mean SF location shifts poleward by  $\sim$ 3° latitude (Figure 6a): under historical forcing (1920–2005), the SF is displaced southward by  $\sim$ 1° latitude and under RCP8.5 forcing (2006–2100), the SF shifts even further south, by an additional  $\sim$ 2° latitude. In Figure 6a, we compare the long-term poleward shift in the ensemble mean position of the zonally averaged SF (black line) to the temporal variance in the SF as simulated by the control integration (representing an unforced climate; blue box and whisker markers). The transient SF lies outside the range of unforced variability of the control SF, highlighting the influence of RCP8.5 external forcing on the SF by the end of the century (i.e., the anthropogenic signal). The intensity of the annual, zonal mean SF, and its associated Si concentration increases from 1920 to 2100, by nearly 0.4 mmol/m³ per 100 km and 0.5 mmol/m³, respectively. Under RCP8.5 forcing, the annual, zonal mean sea surface salinity (SSS) and SST at the SF decreases by  $\sim$ 0.2 g/kg and warms by  $\sim$ 1.5°C, respectively, while the SSH and MLD identified at the SF decreases by  $\sim$ 0.4 m and MLD shoals by more than 5 m, respectively.

Figure 6b displays the total change in the SF between the 2000s and 2090s at all longitudes. We find that the SF shifts poleward, by up to 6° latitude in some regions. The varied magnitude of the shifts across the basin reflect the influence of bottom depth on long-term change in the SF: smallest (and sometimes insignificant) meridional shifts are found in regions characterized by shallow bottom depths, while the largest (and most significant) meridional shifts are found in deeper ocean regions (see also Figure 5). These poleward displacements of the SF are not found to be seasonally dependent, though some regions (e.g., Drake Passage) exhibit a slightly greater displacement in warm season months (summer–fall; not shown).

Why does the SF shift south? We find that a more poleward SF in future, as simulated by the CESM-LE, reflects large-scale changes in Southern Ocean nutrients in a warmer world: a decrease in Si and N at the surface,

19449224, 2018, 5, Downloaded from https://agupubs.onlinelibrary.wiley.com/doi/10.1029/2017GB005816, Wiley Online Library on [22/02/2023]. See the Terms and Conditions (https://onlinelibrary.wiley.com/derms/

conditions) on Wiley Online Library for rules of use; OA articles are governed by the applicable Creative Commons Licenso



**Figure 6.** (a) Time series (1920–2100) of the Community Earth System Model Large Ensemble monthly, zonal, ensemble mean Silicate Front (SF) position (black line;  $\pm 1\sigma$  across the 34 ensemble members indicated by gray shading); the seasonal cycle has been removed by applying a seasonal moving average). Blue boxes at the beginning and end of the time series indicate the zonal, decadal mean SF position as simulated by the control for the 1920s and 2090s, respectively; blue whiskers indicate  $\pm 1\sigma$  in the control zonal mean monthly time series (1920–2100). (b) Total shift in the Community Earth System Model Large Ensemble monthly ensemble mean SF position (negative—southward) between the 2000s and 2090s (reported as an epoch difference). Black bars indicate significance based on the spread (signal:noise) in the ensemble members.

by 2.7 and 1.2 mmol/m³, respectively, between 44° and 65°S (Figure 7). The subsurface SF also shifts poleward in future, but in smaller magnitude, also as a result of decreased Si and N at 200 m in future (not shown). Figure 7 demonstrates that the magnitude of the long-term decrease in Si is greater than that for N, further supporting a more poleward SF in future; indeed, we find long-term decreases in Si:N ratios across the basin. Additionally, we find a long-term intensification of the SF. Across the Southern Ocean, the local gradients in Si increase between the present-day and future positions of the SF; a few regional exceptions include the New Zealand and Scotia Sea sectors, on the windward side of Kerguelen, and at  $\sim$ 20°E, where a southward shift in the SF is marked by a weakening of the background gradients in Si. We discuss possible mechanisms for long-term nutrient decline in the upper 200 m in section 4.1.

## 4. Discussion

In this study, we present an analysis of the large-scale, persistent SF using the CESM-LE simulations, allowing for the separation of natural variability from long-term forced trends under a high-emission scenario. Here we examine the long-term poleward shift of the SF in the context of physical circulation and phytoplankton dynamics. Next, we highlight broader implications and consequences of variability and long-term change in the location of the SF. Lastly, we discuss the limitations of this study.

#### 4.1. A More Poleward SF: Mechanisms and Implications

We assessed long-term change in the position of the surface SF. According to the CESM-LE simulations, the SF shifts south both in zonal average (1920–2100; Figure 6a) and at nearly every longitude (2090s – 2000s; Figure 6b). A more poleward SF can be explained by a combination of physical and biological processes that drive nutrient reductions at the surface (Figure 7).

## 4.1.1. Physical Processes

From present to future, we find that the Southern Ocean surface warms by  $\sim$ 2.5°C, from 5.0 to 7.5°C, respectively (decadal, area-weighted, ensemble mean values between 44–65°S; Figure 8a), with largest warming

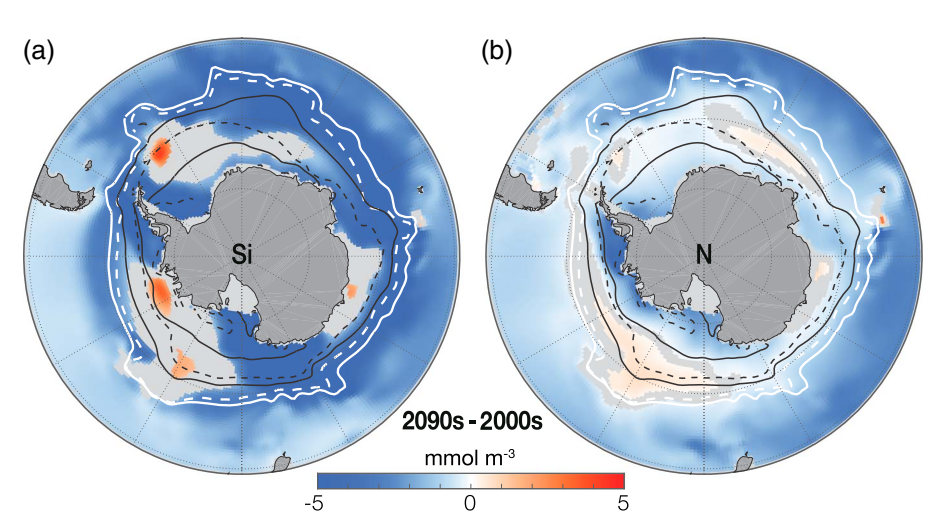


**Figure 7.** Epoch differences (2090s – 2000s) in Community Earth System Model Large Ensemble simulated ensemble mean surface (a) Si and (b) N concentration (colors); only significant changes are shown (see section 2.3). White contours mark the present (solid) and future (dashed) decadal mean positions of the Silicate Front, while the black contours mark the present (solid) and future (dashed) decadal mean maximum (September; most northerly) and minimum (February; most southerly) sea ice extent (see section 2.3).

signals documented in the south-central Indian sector, just east of the Heard and McDonald Islands, by as much as  $\sim$ 5.3°C and the southeast Atlantic sector by  $\sim$ 4.7°C, consistent with other CMIP5 model findings (Cabré et al., 2013). This large-scale warming acts to increase stratification (Figure 8b) and shoal mixed layer depths (MLDs; Figure 8c) across the Southern Ocean, some locations by as much as  $\sim$ 34% and  $\sim$ 54 m, respectively. Warming-induced stratification of the water column would suggest changes in vertical mixing: a warmer, more stratified Southern Ocean at the end of the century likely reduces the vertical supply of nutrients over time, leading to decreased surface Si and N (Figure 7). Concurrently, CESM-LE zonal wind speeds (at 10 m atmospheric height) and wind stress increase significantly across the east Indian and Pacific sectors (not shown), which would suggest a vertical mixing response that would work against any warming-induced stratification: an increase in northward Ekman transport and a subsequent increase in the vertical supply of nutrients from below. An increase in zonal wind speeds and stress would also act to deepen MLDs, yet the robust MLD shoaling across the basin (Figure 8c) suggests that the upper water column's response to external forcing is dominated by increased stratification; ML deepening found nearer the Antarctic continent is likely a result of a reduction in maximum (September) sea ice extent under RCP8.5 forcing (see Figure 8c).

We conclude that warming-induced stratification throughout the 21st century likely explains, in part, reduced Si and N concentrations at the surface and thus a more poleward SF in future. We further speculate that MLD shoaling and nutrient-specific remineralization rates (Broecker & Peng, 1982) help to explain why the long-term reduction in surface Si is greater than that for N (Figure 7) and the vertical gradient in the long-term change in Si is greater than that for N throughout the water column (e.g., Figure 9).

In addition to changes in vertical mixing, any long-term changes in the dynamics of the ACC and its fronts could drive changes in the SF. We use the CESM-LE ensemble mean barotropic stream function to quantify long-term changes in the mean latitude of the core of ACC transport. As in Meijers et al. (2012), the core of the ACC is computed from the barotropic streamfunction by determining a range of transport values relative to the Drake Passage and finding the mean latitude of the upper 50% of zonal transport within that range. Figure 10 shows that the ensemble mean core position of the ACC has remained unchanged under historical and RCP8.5 forcing. In addition to bathymetry, the westerly winds are regarded as a major driver in the position of the ACC and its fronts (e.g., Dong et al., 2006; Graham et al., 2012), but despite a significant long-term increase in the driving westerlies in the east Indian and Pacific sectors (not shown), the position of the Westerly Jet does not shift (not shown; defined as the latitude of the maximum zonal mean wind speed as in Swart et al., 2015) and the result is a persistently stable ACC core from 1920 to 2100. Therefore, the long-term poleward shift in the SF is independent of ACC transport on interdecadal time scales (compare Figures 5 and 10).

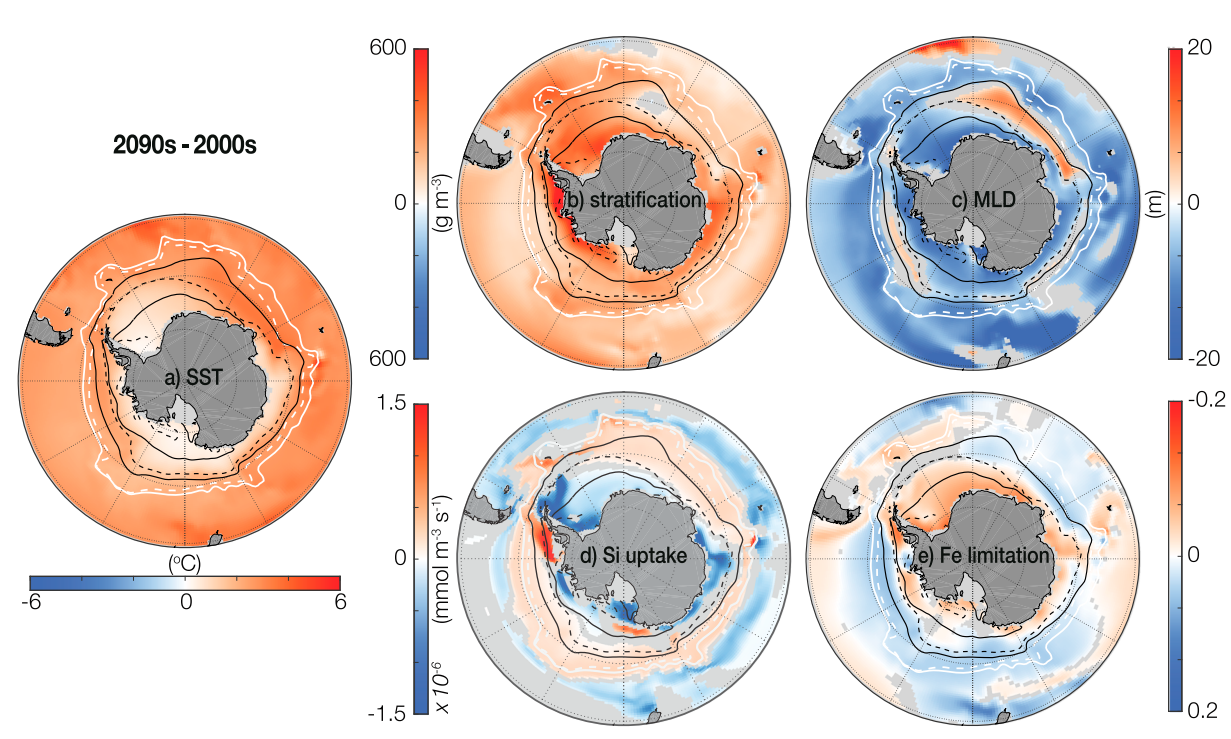
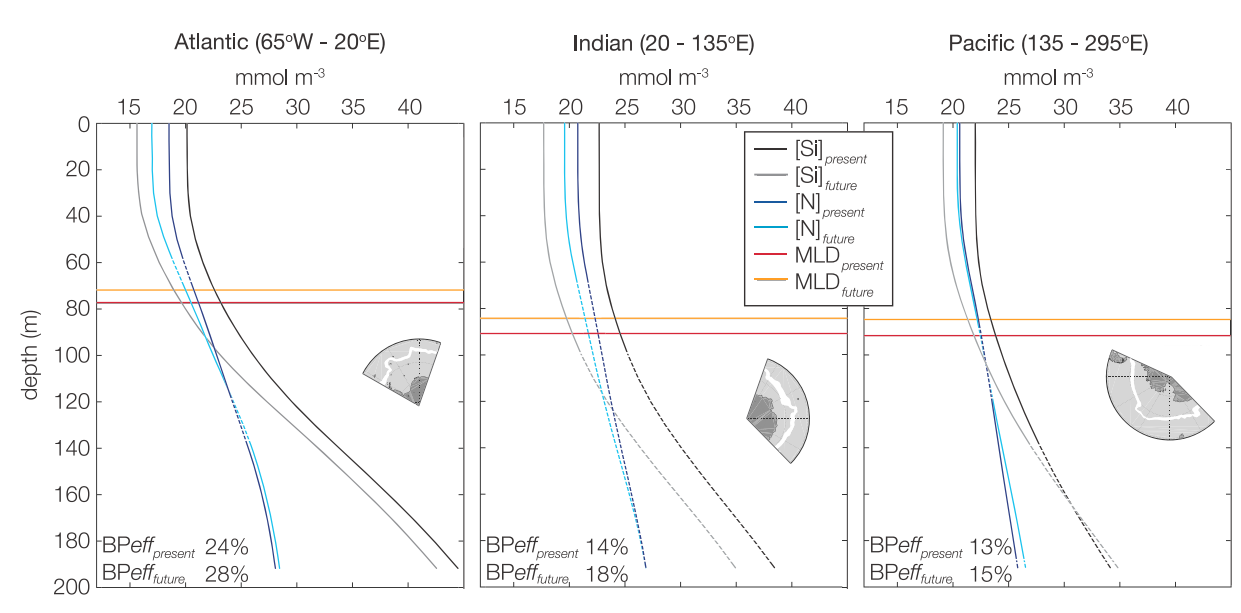


Figure 8. Epoch differences (2090s – 2000s) in Community Earth System Model Large Ensemble simulated ensemble mean surface (a) SST, (b) stratification (defined as the density difference between the surface and 200 m), (c) mixed layer depth (MLD), (d) Si uptake by diatoms, and (e) diatom Fe limitation; only significant changes are shown (see section 2.3), and black and white contours in stereographic plots are the same as in Figure 7. Note that in (e), color has been inverted so that blue colors represent less iron limitation in the future; limitation terms are on a [0, 1] scale, where 0 (1) is most (least) limiting.

Additionally, we examine absolute gradients in SST and SSS to quantify long-term changes in the hydrographic structure of the ACC system (e.g., thermal and haline fronts at the surface). In particular, we investigate changes in the CESM-LE PF; the fundamental dynamical processes that set up the hydrographic PF have long been understood to be the same processes that set up the biogeochemical SF (i.e., that the PF and SF are inherently coupled; see section 1). While the coarse resolution of the CESM-LE precludes a traditional identification of the PF, an objective analysis of  $\nabla$ SST and  $\nabla$ SSS reveals that while the thermal intensity of the PF has increased long term, the CESM-LE ensemble mean PF has not shifted meridionally under RCP8.5 forcing (not shown); any significant long-term changes in  $\nabla$ SST or  $\nabla$ SSS occur in regions where sea ice retreats under climate warming and are therefore not associated with traditional fronts. Given that the SF shifts poleward while the rest of the ACC system, its defining dynamical and hydrographic characteristics or its major drivers (wind, bathymetry), remain unchanged suggests a decoupling of these key dynamical and biogeochemical features of the Southern Ocean, particularly a decoupling of the SF and PF on interdecadal time scales under external (i.e., climate change) forcing. This result highlights a need to further investigate the relationship between the PF and SF in the modern-day Southern Ocean. We discuss the implications of such a decoupling for paleo proxies in section 4.1.3.

## 4.1.2. Biological Processes

Phytoplankton physiology will be directly and indirectly affected by Southern Ocean warming: warming increases phytoplankton growth rates (see Eppley, 1972; Kremer et al., 2017; Moore et al., 2004), while warming-induced stratification limits access to nutrients through a reduction in the vertical supply. While spatially heterogeneous, we observe a significant increase in Si uptake by diatoms within and to the south of the SF over the 21st century (Figure 8d), consistent with studies that have reported increased diatom net primary productivity here (Krumhardt et al., 2017; Leung et al., 2015; Marinov et al., 2010; Misumi et al., 2014), and likely contributing to reduced surface Si (Figure 7a). This positive diatom response is likely driven by warming and reduced iron (Fe) limitation over time (Figure 8e; Misumi et al., 2014; Moore et al., 2013). Misumi et al. (2014) show that elevated Fe supply to the Southern Ocean by the end of the 21st century is largely a result of increased horizontal advection, most notably from an intensified and more poleward large-scale subtropical gyre circulation in the Atlantic sector.



**Figure 9.** Between the latitudes of the present (2000s) and future (2090s) ensemble mean Silicate Front positions (white shaded frontal region in inset map), ensemble mean vertical profiles of present and future Si and N concentration and mixed layer depth (MLD) in the upper 200 m in the Atlantic, Indian, and Pacific sectors of the Southern Ocean as simulated by the Community Earth System Model Large Ensemble; at depth, dashes indicate where model drift relative to the reported change in that nutrient cannot be deemed negligible. Present and future ensemble mean biological pump efficiency (BP*eff*), with respect to N concentration, is reported for each region (lower left of each panel; defined as  $\frac{|N|_d - |N|_s}{|N|_d - |N|_s}$ , where subscripts s and d indicate the average concentration of the surface (0–100 m) and deep (100–200 m) layers, respectively; Sarmiento & Gruber, 2006).

Small phytoplankton are more competitive for nutrients at low concentrations; their larger surface area-to-volume ratio is parameterized in the CESM via prescribed half-saturation coefficients for nutrient uptake. While diatoms and small phytoplankton have been prescribed the same maximum growth rates in the CESM-LE, for a given increase of Fe to an iron-limited system, the growth rate response of diatoms will be greater than that of small phytoplankton. Therefore, it is likely that some portion of the long-term decrease in surface macronutrients (Figure 7) is attributable to increased diatom productivity and utilization of Si here (Figure 8d; that is, a more efficient biological pump; Figure 9) driven by reduced Fe limitation (Figure 8e; Wang et al., 2017). Independent of the location of the SF, a lower Si:N across the Southern Ocean in future has implications for the relative abundance of diatoms versus nonsiliceous phytoplankton, likely leading regime shifts in phytoplankton community structure (see John et al., 2015).

#### 4.1.3. The SF on Glacial-Interglacial Time Scales

The modern-day relationship between diatom productivity and export in the silicate-replete Antarctic waters south of the PF and the opal-dominated sediments below (i.e., the Opal Belt; e.g., DeMaster, 1981) has been used to infer changes in diatom productivity and the air-sea carbon balance on glacial-interglacial time scales (e.g., Abelmann et al., 2006; Anderson et al., 2009; Crosta et al., 2004; Kemp et al., 2010; Kohfeld et al., 2013; Nair et al., 2015; Taylor-Silva & Riesselman, 2018). Whether the PF was displaced significantly north or south from its modern-day position on these time scales is still a topic of debate (see Kemp et al., 2010). Results from this study suggest that on a near-centennial time scale, the SF can vary by up to  $\sim$ 6° latitude in regions not characterized by shallow bathymetry (Figure 6b). However, the poleward shift in the SF reported here is independent of the PF, suggesting a decoupling of these biogeochemical and hydrographic fronts on interdecadal time scales and highlighting the need for a re-evaluation of the relationship of these key frontal features.

## 4.2. Study Limitations and Caveats

Unlike the observed complex frontal structure of the PF, which can split into multiple filaments in regions characterized by deeper bottom depths (Graham et al., 2012; Sokolov & Rintoul, 2002), the SF identified in this study is generally located at one latitudinal point at a given longitudinal position (by nature, rather than by choice or mapping scheme) and influenced by a documented low nutrient bias (Moore et al., 2013). We acknowledge that our SF analysis lacks information on smaller scales of variability, owing to the coarse resolution of the CESM (~1°), and thus omits mesoscale or submesoscale features. Currently, the importance of small scales of variability on the SF is unknown owing to a lack of observational metrics. While this study boasts

19449224, 2018, 5, Downloaded from https://agupubs.onlinelibrary.wiley.com/doi/10.1029/2017GB005816, Wiley Online Library on [22/02/2023]. See the Terms and Conditions (https://onlinelibrary.wiley.com/derms/

-conditions) on Wiley Online Library for rules of use; OA articles are governed by the applicable Creative Commons Licens

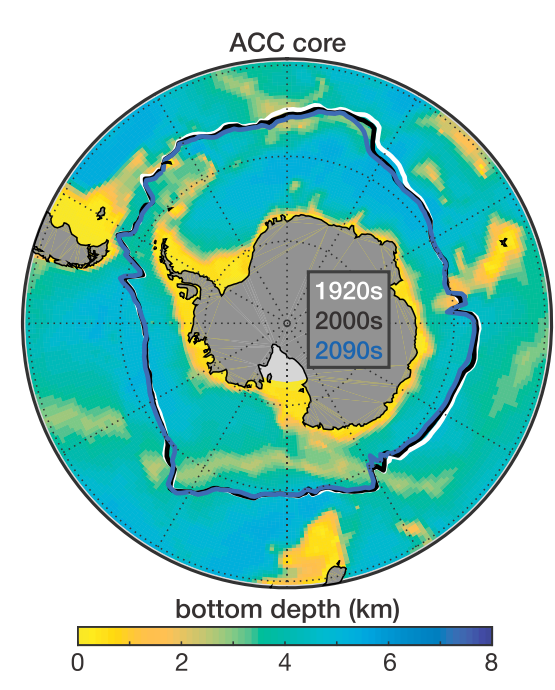


**Figure 10.** Decadal mean Antarctic Circumpolar Current (ACC) core positions (defined after Meijers et al., 2012): historical (1920s; white contour), present-day (2000s; black contour), and future (2090s; blue contour) ensemble mean location. Community Earth System Model version 1 bathymetry displayed underneath Silicate Front positions in color, where warm colors indicate shallow bathymetry and cool colors indicate deep.

the ability to address the role of internal climate variability by using a large ensemble, we cannot address the role of model structural uncertainty in long-term SF trends (Lovenduski et al., 2016).

Model drift (i.e., long-term change in the control simulation), if present, indicates that a tracer field is not at equilibrium with respect to the physical circulation, owing to insufficient and often infeasible model spin-up time prior to transient runs, a common issue plaguing model experiments (see Séférian et al., 2016). Despite drift in the simulated surface concentrations of Si and N (-0.42 and -0.20 mmol/m³ epoch differences, respectively) the long-term large-scale decrease in surface macronutrients and latitude of the SF reported here is robust. For example, the overlap of the blue whiskers in Figure 6a indicates that the historical and future SF latitudes from the control are not statistically indistinguishable and therefore the long-term change in the control SF (i.e., model drift in the SF) is not significant, yielding a robust climatic change in the transient SF.

Like many Earth System Models, the CESM model has been tuned to approximately match observations of nutrient fields. In particular, the supply and removal of Fe in these models remains poorly constrained (Tagliabue et al., 2016).

Given the known importance of silicate availability for diatom growth and the SF as a key biogeochemical divide, we speculate that diatom production would decrease, relative to present day, as a consequence of a significant poleward shift in the SF. Ecologically, significant changes in the position of the SF would have implications for Southern Ocean biogeography, associated with shifts in the base of the marine food chain (e.g., from diatoms to small phytoplankton), with subsequent impacts on biodiversity (see Conversi et al., 2015; John et al., 2015; Schabhüttl et al., 2013). Here the CESM-LE simulates an increase in diatom productivity by the 2090s despite a more poleward SF, likely owing to the current configuration of the BEC model: nutrient limitation terms and half-saturation constants (Km terms) are prescribed in a way that results in a dominance of Fe limitation across the Southern Ocean, to the point that diatoms do not respond to simulated changes in Si and thus the position of the SF (Km for Si likely too low in BEC). In reality, we could expect diatoms to experience and respond to Si limitation and Fe colimitation in the Southern Ocean, particularly near the SF (Cortese & Gersonde, 2008; Hoffmann et al., 2008). Indeed, some microcosm and open Southern Ocean studies suggest that Si is a major driver in the partitioning of diatoms versus smaller phytoplankton (e.g., coccolithophores; Egge & Aksnes, 1992; Eynaud et al., 1999; Mohan et al., 2008). Our results highlight a need to better represent and investigate the relationship between the SF and biogeography in climate models.

## 5. Conclusions

We use the CESM-LE simulations to quantify the temporal variability of the Southern Ocean SF and its response to 21st century warming. In summary, this study finds that the latitudinal location of the SF is influenced by biology and bathymetry. On seasonal time scales, biology largely determines the location of the SF, in its northernmost position in austral winter and southernmost in austral summer, reflecting seasonal diatom utilization of Si and N. On interannual to interdecadal time scales, Southern Ocean bathymetry largely determines the location of the SF, acting to limit its meridional extent and temporal variance over shallow regions. Under historical and RCP8.5 forcing, the SF shifts poleward both in zonal average and at nearly every longitude, with largest poleward displacements in deep-ocean regions. A more poleward SF cannot be explained by a shift in the Antarctic PF or the core of ACC transport. We attribute a more poleward SF to a combination of physical and biological mechanisms that drive reduced macronutrients at the surface: a reduction in the vertical supply of Si and N driven by a robust warming-induced stratification and an increase in Si used by diatoms driven by reduced iron limitation over time.

#### Acknowledgments

This work has benefited from discussions with Peter R. Gent and Thomas M. Marchitto. We thank the ARSV Laurence M. Gould marine and science support teams for their collection of discrete samples (found at www.ldeo.columbia.edu/res/pi/CO2/ carbondioxide/pages/global\_ph.html); nutrient analyses were performed at Chesapeake Biological Laboratory and the Oceanographic Data Facility at Scripps Institution of Oceanography, University of California San Diego. WOA13 climatological nutrients are available at http://nodc.noaa.gov/ OC5/woa13/. CMIP5 output is provided by the World Data Center for Climate (http://cera-www.dkrz.de). CESM-LE output is available from the Earth System Grid at www.earthsystemgrid. org/dataset/ucar.cgd.ccsm4. CESM\_CAM5\_BGC\_LE.html. CESM computing resources were provided by CISL at NCAR: NCAR is sponsored by NSF. We are grateful for funding from NSF (PLR-1543457, OCE-1558225, OCE-1258995, and OCE-1155240) and NOAA (NA12OAR4310058).

#### References

- Abelmann, A., Gersonde, R., Cortese, G., Kuhn, G., & Smetacek, V. (2006). Extensive phytoplankton blooms in the Atlantic sector of the glacial Southern Ocean. *Paleoceanography*, 21, PA1013. https://doi.org/10.1029/2005PA001199
- Anderson, R. F., Ali, S., Bradtmiller, L. I., Nielsen, S. H. H., Fleisher, M. Q., Anderson, B. E., & Burckle, L. H. (2009). Wind-driven upwelling in the Southern Ocean and the deglacial rise in atmospheric CO<sub>2</sub>. Science, 323(5920), 1443–1448. https://doi.org/10.1126/science.1167441
- Balch, W. M., Bates, N. R., Lam, P. J., Twining, B. S., Rosengard, S. Z., Bowler, B. C., et al. (2016). Factors regulating the Great Calcite Belt in the Southern Ocean and its biogeochemical significance. *Global Biogeochemical Cycles*, *30*, 1124–1144. https://doi.org/10.1002/2016GB005414
- Bates, S. C., Fox-Kemper, B., Jayne, S. R., Large, W. G., Stevenson, S., & Yeager, S. G. (2012). Mean biases, variability, and trends in air-sea fluxes and sea surface temperature in the CCSM4. *Journal of Climate*, 25, 7781 7801. https://doi.org/10.1175/JCLI-D-11-00442.1
- Belkin, I. M., & Gordon, A. L. (1996). Southern Ocean fronts from the Greenwich meridian to Tasmania. *Journal of Geophysical Research*, 101, 3675–3696
- Boyer, T. P., Antonov, J. I., Baranova, O. K., Coleman, C., Garcia, H. E., Grodsky, A., et al. (2013). World Ocean Database 2013. no. 72 in NOAA
- Broecker, W. S., & Peng, T.-H. (1982). Tracers in the sea. Palisades, NY: A publication of the Lamont-Doherty Geological Observatory.
- Cabré, A., Leung, S., & Marinov, I. (2013). Southern Ocean response to climate change in the CMIP5 models: Linking biology to physics. Paper presented at Carbon-Climate Connections in the Earth System. NCAR. Boulder. CO. 7 August.
- Chelton, D. B., Schlax, M. G., Witter, D. L., & Richman, J. G. (1990). Geosat altimeter observations of the surface circulation of the Southern Ocean. *Journal of Geophysical Research*, 95(C10), 17,877 17,903. https://doi.org/10.1029/JC095iC10p17877
- Collins, W. J., Bellouin, N., Doutriaux-Boucher, M., Gedney, N., Halloran, P., Hinton, T., et al. (2011). Development and evaluation of an Earth-system model—HadGEM2. Geoscientific Model Development, 4(4), 1051–1075. https://doi.org/10.5194/gmd-4-1051-2011
- Conversi, A., Dakos, V., Grdmark, A., Ling, S., Folke, C., Mumby, P. J., et al. (2015). A holistic view of marine regime shifts. *Philosophical Transactions of the Royal Society B*, 370, 20130279. https://doi.org/10.1098/rstb.2013.0279
- Cortese, G., & Gersonde, R. (2008). Plio/Pleistocene changes in the main biogenic silica carrier in the Southern Ocean, Atlantic Sector. *Marine Geology*, 252, 100–110. https://doi.org/10.1016/j.margeo.2008.03.015
- Crosta, X., Sturm, A., Armand, L., & Pichon, J.-J. (2004). Late Quaternary sea ice history in the Indian sector of the Southern Ocean as recorded by diatom assemblages. *Marine Micropaleontology*, 50, 209–223. https://doi.org/10.1016/S0377-8398(03)00072-0
- Cunningham, S. A., Alderson, S. G., & King, B. A. (2003). Transport and variability of the Antarctic Circumpolar Current in Drake Passage. Journal of Geophysical Research, 108(C5), 8084. https://doi.org/10.1029/2001JC001147
- Danabasoglu, G., Bates, S. C., Briegleb, B. P., Jayne, S. R., Jochum, M., Large, W. G., et al. (2012). The CCSM4 ocean component. *Journal of Climate*, 25(5), 1361–1389. https://doi.org/10.1175/JCLI-D-11-00091.1
- Deacon, G. E. R. (1937). The hydrology of the Southern Ocean. Discovery reports (pp. 1-124). London: Cambridge University Press.
- Deacon, G. E. R. (1982). Physical and biological zonation in the Southern Ocean. *Deep-Sea Research*, 29(1), 1–15. https://doi.org/10.1016/0198-0149(82)90058-9
- DeMaster, D. J. (1981). The supply and accumulation of silica in the marine environment. *Geochimica et Cosmochimica Acta*, 45, 1715–1732. DeMaster, D. J. (2002). The accumulation and cycling of biogenic silica in the Southern Ocean: Revisiting the marine silica budget. *Deep-Sea Research*, 49(16), 3155–3167.
- Doney, S. C., Lindsay, K., Fung, I., & John, J. (2006). Natural variability in a stable, 1000-yr global coupled climate-carbon cycle simulation. Journal of Climate, 19(13), 3033–3054. https://doi.org/10.1175/JCLI3783.1
- Dong, S., Sprintall, J., & Gille, S. T. (2006). Location of the Antarctic Polar Front from AMSR-E Satellite sea surface temperature measurements. Journal of Physical Oceanography, 36, 2075–2089.
- Donohue, K. A., Tracey, K. L., Watts, D. R., Chidichimo, M. P., & Chereskin, T. K. (2016). Mean Antarctic Circumpolar Current transport measured in Drake Passage. *Geophysical Research Letters*, 43, 760–767. https://doi.org/10.1002/2016GL070319
- Dunne, J. P., John, J. G., Adcroft, A. J., Griffies, S. M., Hallberg, R. W., Shevliakova, E., et al. (2012). GFDL's ESM2 global coupled climate-carbon Earth system models. Part I: Physical formulation and baseline simulation characteristics. *Journal of Climate*, 25, 6646–6665. https://doi.org/10.1175/JCLI-D-11-00560.1
- Dunne, J. P., John, J. G., Shevliakova, E., Stouffer, R. J., Krasting, J. P., Malyshev, S. L., et al. (2013). GFDL's ESM2 global coupled climate-carbon Earth system models. Part II: Carbon system formulation and baseline simulation characteristics. *Journal of Climate*, 26, 2247–2267. https://doi.org/10.1175/JCLI-D-12-00150.1
- Egge, J. K., & Aksnes, D. L. (1992). Silicate as regulating nutrient in phytoplankton competition. *Marine Ecology Progress Series*, 83(2–3), 281–289.
- Eppley, R. W. (1972). Temperature and phytoplankton growth in the sea. Fishery Bulletin, 70(4), 1063 1085.

- Eynaud, F., Giraudeau, J., Pichon, J.-J., & Pudsey, C. J. (1999). Sea-surface distribution of coccolithophores, diatoms, silicoflagellates and dinoflagellates in the South Atlantic Ocean during the late austral summer 1995. *Deep-Sea Research*, 46(3), 451–482.
- Farneti, R., Downes, S. M., Griffies, S. M., Marsland, S. J., Behrens, E., Bentsen, M., et al. (2015). An assessment of Antarctic Circumpolar Current and Southern Ocean meridional overturning circulation during 1958–2007 in a suite of interannual CORE-II simulations. *Ocean Modelling*, 93, 84–120. https://doi.org/10.1016/j.ocemod.2015.07.009
- Franck, V. M., Brzezinski, M. A., Coale, K. H., & Nelson, D. M. (2000). Iron and silicic acid concentrations regulate Si uptake north and south of the Polar Frontal Zone in the Pacific sector of the Southern Ocean. *Deep-Sea Research*, 47(15-16), 3315–3338.
- Freeman, N. M., & Lovenduski, N. S. (2016). Mapping the Antarctic Polar Front: Weekly realizations from 2002 to 2014. Earth System Science Data, 8, 191 198. https://doi.org/10.5194/essd-8-191-2016
- Freeman, N. M., Lovenduski, N. S., & Gent, P. R. (2016). Temporal variability in the Antarctic Polar Front (2002–2014). *Journal of Geophysical Research: Oceans*, 121, 7263–7276. https://doi.org/10.1002/2016JC012145
- Garcia, H. E., Locarnini, R. A., Boyer, T. P., Antonov, J. I., Baranova, O. K., Zweng, M. M., et al. (2013). World Ocean Atlas 2013. Vol. 4: Dissolved Inorganic Nutrients (phosphate, nitrate, silicate). In S. Levitus & A. Mishonov (Eds.), NOAA Atlas NESDIS 76 (25 pp.).
- Gent, P. R., & McWilliams, J. C. (1990). Isopycnal mixing in ocean circulation models. Journal of Physical Oceanography, 20, 150-155.
- Gent, P. R., Willebrand, J., McDougall, T. J., & McWilliams, J. C. (1995). Parameterizing eddy-induced tracer transports in ocean circulation models. *Journal of Physical Oceanography*, 25, 463–474.
- Gille, S. T. (1994). Mean sea surface height of the Antarctic Circumpolar Current from Geosat data: Method and application. *Journal of Geophysical Research*, 99, 255–273.
- Giorgetta, M. A., Jungclaus, J., Reick, C. H., Legutke, S., Bader, J., Böttinger, M., et al. (2013). Climate and carbon cycle changes from 1850 to 2100 in MPI-ESM simulations for the Coupled Model Intercomparison Project phase 5. *Journal of Advances in Modeling Earth Systems*, 5, 572–597. https://doi.org/10.1002/jame.20038
- Gordon, A. L., Molinelli, E., & Baker, T. (1978). Large-scale relative dynamic topography of the Southern Ocean. *Journal of Geophysical Research*, 83(C6), 3023–3032.
- Graham, R. M., De Boer, A. M., Heywood, K. J., Chapman, M. R., & Stevens, D. P. (2012). Southern Ocean fronts: Controlled by wind or topography? *Journal of Geophysical Research*, 117, C08018. https://doi.org/10.1029/2012JC007887
- HadGEM2 Development Team (2011). The Had GEM2 family of Met Office Unified Model climate configurations. *Geoscientific Model Development*, 4(3), 723–757. https://doi.org/10.5194/qmd-4-723-2011
- Hoffmann, L. J., Peeken, I., & Lochte, K. (2008). Iron, silicate, and light co-limitation of three Southern Ocean diatom species. *Polar Biology*, 31, 1067 1080. https://doi.org/10.1007/s00300-008-0448-6
- Hunke, E., & Lipscomb, W. (2008). CICE: The Los Alamos sea ice model, documentation and software user's manual, version 4.0, Los Alamos National Laboratory. Los Alamos. New Mexico.
- Hurrell, J. W., Holland, M. M., & Gent, P. R. (2013). The Community Earth System Model: A framework for collaborative research. *Bulletin of the American Meteorological Society*, 94, 1339–1360. https://doi.org/10.1175/BAMS-D-12-00121.1
- Ilyina, T., Six, K. D., Segschneider, J., Maier-Reimer, E., Li, H., & Nunez-Riboni, I. (2013). Global ocean biogeochemistry model HAMOCC: Model architecture and performance as component of the MPI-Earth system model in different CMIP5 experimental realizations. *Journal of Advances in Modeling Earth Systems*, 5, 287–315. https://doi.org/10.1029/2012MS000178
- John, J. G., Stock, C. A., & Dunne, J. P. (2015). A more productive, but different, ocean after mitigation. *Geophysical Research Letters*, 42, 9836–9845. https://doi.org/10.1002/2015GL066160
- Kay, J. E., Deser, C., Phillips, A., Mai, A., Hannay, C., Strand, G., et al. (2015). The Community Earth System Model (CESM) Large Ensemble Project: A community resource for studying climate change in the presence of internal climate variability. *Bulletin of the American Meteorological Society*, 96, 1333–1349. https://doi.org/10.1175/BAMS-D-13-00255.1
- Kemp, A. E. S., Grigorov, I., Pearce, R. B., & Naveira Garabato, A. C. (2010). Migration of the Antarctic Polar Front through the mid-Pleistocene transition: Evidence and climatic implications. *Quarternary Science Reviews*, 29, 1993–2009.
- Kohfeld, K. E., Graham, R. M., de Boer, A. M., Sime, L. C., Wolff, E. W., Le Quéré, C., & Bopp, L. (2013). Southern Hemisphere westerly wind changes during the Last Glacial Maximum: Paleo-data synthesis. *Quarternary Science Reviews*, 68, 76–95. https://doi.org/10.1016/j.guascirev.2013.01.017
- Kremer, C. T., Thomas, M. K., & Litchman, E. (2017). Temperature- and size-scaling of phytoplankton population growth rates: Reconciling the Eppley curve and the metabolic theory of ecology. *Limnology and Oceanography*, 62, 1658–1670. https://doi.org/10.1002/lno.10523
- Krumhardt, K. M., Lovenduski, N. S., Long, M. C., & Lindsay, K. (2017). Avoidable impacts of ocean warming on marine primary production: Insights from the CESM ensembles. *Global Biogeochemical Cycles*, *31*, 114–133. https://doi.org/10.1002/2016GB005528
- Krzywinski, M., & Altman, N. (2014). Points of significance: Visualizing samples with box plots. *Nature Methods*, 11, 119–120. https://doi.org/10.1038/nmeth.2813
- Leung, S., Cabré, A., & Marinov, I. (2015). A latitudinally banded phytoplankton response to 21st century climate change in the Southern Ocean across the CMIP5 model suite. *Biogeosciences*, 12, 5715–5734. https://doi.org/10.5194/bg-12-5715-2015
- Leynaert, A., Bucciarelli, E., Claquin, P., Dugdale, R. C., Martin-Jézéquel, V., Pondaven, P., & Ragueneau, O. (2004). Effect of iron deficiency on diatom cell size and silicic acid uptake kinetics. *Limnology and Oceanography*, 49(41), 1134–1143.
- Long, M. C., Lindsay, K., Peacock, S., Moore, J. K., & Doney, S. C. (2013). Twentieth-century oceanic carbon uptake and storage in CESM1(BGC)\*. *Journal of Climate*, 26, 6775–6800.
- Lovenduski, N. S., McKinley, G. A., Fay, A. R., Lindsay, K., & Long, M. C. (2016). Partitioning uncertainty in ocean carbon uptake projections: Internal variability, emission scenario, and model structure. *Global Biogeochemical Cycles*, 30, 1276–1282. https://doi.org/10.1002/2016GB005426
- Marinov, I., Gnanadesikan, A., Toggweiler, J. R., & Sarmiento, J. L. (2006). The Southern Ocean biogeochemical divide. *Nature*, 441(7096), 964–967
- Marinov, I., Doney, S. C., & Lima, I. D. (2010). Response of ocean phytoplankton community structure to climate change over the 21st century: Partitioning the effects of nutrients, temperature and light. *Biogeosciences*, 7(12), 3941–3959. https://doi.org/10.5194/bg-6-3941-2010
- McKinley, G. A., Pilcher, D. J., Fay, A. R., Lindsay, K., Long, M. C., & Lovenduski, N. S. (2016). Timescales for detection of trends in the ocean carbon sink. *Nature*, 530, 469–472.
- McKinley, G. A., Fay, A. R., Lovenduski, N. S., & Pilcher, D. J. (2017). Natural variability and anthropogenic trends in the ocean carbon sink. Annual Review of Marine Science, 9, 125–150. https://doi.org/10.1146/annurev-marine-010816-060529
- Meijers, A. J. S., Shuckburgh, E., Bruneau, N., Sallée, J. B., Bracegirdle, T. J., & Wang, Z. (2012). Representation of the Antarctic Circumpolar Current in the CMIP5 climate models and future changes under warming scenarios. *Journal of Geophysical Research*, 117, C12008. https://doi.org/10.1029/2012JC008412

- Misumi, K., Lindsay, K., Moore, J. K., Doney, S. C., Bryan, F. O., Tsumune, D., & Yoshida, Y. (2014). The iron budget in ocean surface waters in the 20th and 21st centuries: Projections by the Community Earth System Model version 1. *Biogeosciences*, 11, 33–55. https://doi.org/10.5194/bq-11-33-2014
- Mohan, R., Mergulhao, L. P., Guptha, M. V., Rajakumar, A., Thamban, M., AnilKumar, N., et al. (2008). Ecology of coccolithophores in the Indian sector of the Southern Ocean. *Marine Micropaleontology*, 67, 30–45. https://doi.org/10.1016/j.marmicro.2007.08.005
- Moore, J. K., & Abbott, M. R. (2000). Phytoplankton chlorophyll distributions and primary production in the Southern Ocean. *Journal of Geophysical Research*, 105(C12), 28,709–28,722. https://doi.org/10.1029/1999JC000043
- Moore, J. K., & Bracuher, O. (2008). Sedimentary and mineral dust sources of dissolved iron to the world ocean. *Biogeosciences*, *5*(3), 631–656. https://doi.org/10.5194/bg-5-631-2008
- Moore, J. K., Abbott, M. R., & Richman, J. G. (1999). Location and dynamics of the Antarctic Polar Front from satellite sea surface temperature data. *Journal of Geophysical Research*, 104(C2), 3059–3073. https://doi.org/10.1029/1998JC900032
- Moore, J. K., Doney, S. C., & Lindsay, K. (2004). Upper ocean ecosystem dynamics and iron cycling in a global three-dimensional model. Global Biogeochemical Cycles, 18, GB4028. https://doi.org/10.1029/2004GB002220
- Moore, J. K., Lindsay, K., Doney, S. C., Long, M. C., & Misumi, K. (2013). Marine ecosystem dynamics and biogeochemical cycling in the Community Earth System Model [CESM1(BGC)]: Comparison of the 1990s with the 2090s under the RCP4.5 and RCP8.5 scenarios. Journal of Climate, 26(23), 9291–9312. https://doi.org/10.1175/JCLI-D-12-00566.1
- Munro, D. R., Lovenduski, N. S., Takahashi, T., Stephens, B. B., Newberger, T., & Sweeney, C. (2015). Recent evidence for a strengthening CO<sub>2</sub> sink in the Southern Ocean from carbonate system measurements in the Drake Passage (2002–2015). *Geophysical Research Letters*, 42, 7623–7630. https://doi.org/10.1002/2015GL065194
- Munro, D. R., Lovenduski, N. S., Stephens, B. B., Newberger, T., Arrigo, K. R., Takahashi, T., et al. (2015). Estimates of net community production in the Southern Ocean determined from time series observations (2002–2011) of nutrients, dissolved inorganic carbon, and surface ocean pCO<sub>2</sub> in Drake Passage. Deep-Sea Research, 114, 49–63. https://doi.org/10.1016/j.dsr2.2014.12.014
- Nair, A., Mohan, R., Manoj, M. C., & Thamban, M. (2015). Glacial-interglacial variability in diatom abundance and valve size: Implications for Southern Ocean paleoceanography. *Paleoceanography*, 30, 1245–1260. https://doi.org/10.1002/2014PA002680
- Nelson, D. M., Brzezinski, M. A., Sigmon, D. E., & Franck, V. M. (2001). A seasonal progression of Si limitation in the Pacific sector of the Southern Ocean. *Deep Sea Research Part II: Topical Studies in Oceanography*, 48(19–20), 3973–3995. https://doi.org/10.1016/S0967-0645(01)00076-5
- Orsi, A. H., Whitworth, T. III, & Nowlin, W. D., Jr. (1995). On the meridional extent and fronts of the Antarctic Circumpolar Current. *Deep Sea Research Part I: Oceanographic Research Papers*, 42(5), 641–673. https://doi.org/10. 1016/0967-0637(95)00021-W
- Palmer, J. R., & Totterdell, I. J. (2001). Production and export in a global ocean ecosystem model. *Deep Sea Research Part I: Oceanographic Research Papers*, 48(5), 1169–1198.
- Palter, J. B., Sarmiento, J. L., Gnanadesikan, A., Simeon, J., & Slater, R. D. (2010). Fueling export production: Nutrient return pathways from the deep ocean and their dependence on the Meridional Overturning Circulation. *Biogeosciences*, 7(11), 3549–3568. https://doi.org/10.5194/bg-7-3549-2010
- Palter, J. B., Marinov, I., Sarmiento, J. L., & Gruber, N. (2013). Large-scale, persistent nutrient fronts of the World Ocean: Impacts on biogeochemistry. In I. M. Belkin (Ed.), *Chemical oceanography of frontal zones*. Berlin: Springer-Verlag.
- Pollard, R. T., Lucas, M. I., & Read, J. F. (2002). Physical controls on biogeochemical zonation in the Southern Ocean. *Deep Sea Research Part II: Topical Studies in Oceanography*, 49(16), 3289–3305.
- Pondaven, P., Ragueneau, O., Tréguer, P. J., Hauvespre, A., Dezileau, L., & Reyss, J. L. (2000). Resolving the 'opal paradox' in the Southern Ocean. *Nature*, 405, 168–172.
- Ragueneau, O., Tréguer, P., Leynaert, A., Anderson, R. F., Brzezinski, M. A., DeMaster, D. J., et al. (2000). A review of the Si cycle in the modern ocean: Recent progress and missing gaps in the application of biogenic opal as a paleoproductivity proxy. *Global and Planetary Change*, 26(4), 317–365. https://doi.org/10.1016/S0921-8181(00)00052-7
- Sallée, J. B., Speer, K., & Morrow, R. (2008). Response of the Antarctic Circumpolar Current to atmospheric variability. *Journal of Climate*, 21(12), 3020–3039.
- Sarmiento, J. L., & Gruber, N. (2006). Ocean biogeochemical dynamics. Princeton: Princeton University Press.
- Sarmiento, J. L., Gruber, N., Brzezinski, M. A., & Dunne, J. P. (2004). High-latitude controls of thermocline nutrients and low latitude biological productivity. *Nature*, 427, 56–60.
- Schabhüttl, S., Hingsamer, P., Weigelhofer, G., Hein, T., Weigert, A., & Striebel, M. (2013). Temperature and species richness effects in phytoplankton communities. *Oecologia*, 171, 527 536. https://doi.org/10.1007/s00442-012-2419-4
- Séférian, R., Gehlen, M., Bopp, L., Resplandy, L., Orr, J. C., Marti, O., et al. (2016). Inconsistent strategies to spin up models in CMIPS: Implications for ocean biogeochemical model performance assessment. *Geoscientific Model Development*, *9*, 1827–1851. https://doi.org/10.5194/gmd-9-1827-2016
- Smetacek, V. (1999). Diatoms and the ocean carbon cycle. *Protist*, 150, 25–32.
- Smetacek, V., de Barr, H. J. W., Bathmann, U. V., Lochte, K., & Rutgers van der Loeff, M. M. (1997). Ecology and biogeochemistry of the Antarctic Circumpolar Current during austral spring: A summary of Southern Ocean JGOFS cruise ANT X/6 of R.V. Polarstern. *Deep Sea Research Part II: Topical Studies in Oceanography*, 44(1–2), 1–21.
- Smith, R. D., Jones, P., Briegleb, B., Bryan, F., Danabasoglu, G., Dennis, J., et al. (2010). *The Parallel Ocean Program (POP) reference manual*. Los Alamos, New Mexico: Los Alamos National Laboratory. Retrieved from http://www.cesm.ucar.edu/models/cesm1.0/pop2/doc/sci/POPRefManual.pdf
- Smith Jr., W. O., Anderson, R. F., Moore, J. K., Codispoti, L. A., & Morrison, J. M. (2000). The US Southern Ocean Joint Global Ocean Flux Study: An introduction to AESOPS. Deep Sea Research Part II: Topical Studies in Oceanography, 47(15-16), 3073 3093.
- Sokolov, S., & Rintoul, S. R. (2002). Structure of Southern Ocean fronts at 140° E. Journal of Marine Systems, 37, 151 184.
- Sokolov, S., & Rintoul, S. R. (2007). On the relationship between fronts of the Antarctic Circumpolar Current and surface chlorophyll concentrations in the Southern Ocean. *Journal of Geophysical Research*, 112, C07030. https://doi.org/10.1029/2006jc004072
- Sokolov, S., & Rintoul, S. R. (2009a). Circumpolar structure and distribution of the Antarctic Circumpolar Current fronts: 1. Mean circumpolar paths. *Journal of Geophysical Research*, 114, C11018. https://doi.org/10.1029/2008JC005108
- Sokolov, S., & Rintoul, S. R. (2009b). Circumpolar structure and distribution of the Antarctic Circumpolar Current fronts: 2. Variability and relationship to sea surface height. *Journal of Geophysical Research*, 14, C11019. https://doi.org/10.1029/2008JC005248
- Swart, N. C., Fyfe, J. C., Gillett, N., & Marshall, G. J. (2015). Comparing trends in the Southern Annular Mode and surface westerly jet. *Journal of Climate*, 28, 8840–8859. https://doi.org/10.1175/JCLI-D-15-0334.1

- Tagliabue, A., Mtshali, T., Aumont, O., Bowie, A. R., Klunder, M. B., Roychoudhury, A. N., & Swart, S. (2012). A global compilation of dissolved iron measurements: Focus on distributions and processes in the Southern Ocean. *Biogeosciences*, *9*, 2333–2349. https://doi.org/10.5194/bg-9-2333-2012
- Tagliabue, A., Aumont, O., DeAth, R., Dunne, J. P., Dutkiewicz, S., Galbraith, E., et al. (2016). How well do global ocean biogeochemistry models simulate dissolved iron distributions?. *Global Biogeochemical Cycles*, 30, 149–174. https://doi.org/10.1002/2015GB005289
- Taylor, K. E., Stouffer, R. J., & Meehl, G. A. (2012). An overview of CMIP5 and the experiment design. *Bulletin of the American Meteorological Society*, 93, 485–498. https://doi.org/10.1175/BAMS-D-11-00094.1
- Taylor-Silva, B. I., & Riesselman, C. R. (2018). Polar frontal migration in the warm late Pliocene: Diatom evidence from the Wilkes Land margin, East Antarctica. *Paleoceanography and Paleoclimatology*, 33, 76–92. https://doi.org/10.1002/2017PA003225
- Tréguer, P., Nelson, D. M., Van Bennekom, A. J., DeMaster, D. J., Leynaert, A., & Queguiner, B. (1995). The silica balance in the world ocean: A Reestimate. Science, 268(5209), 375–379. https://doi.org/10.1126/science.268. 5209.375
- Tréguer, P. J. (2014). The Southern Ocean silica cycle. Comptes Rendus Geoscience, 346, 279–286. https://doi.org/10.1016/j.crte.2014.07.003 Wang, Z. T., Sigman, D. M., Prokopenko, M. G., Adkins, J. F., Robinson, L. F., Hines, S. K., et al. (2017). Deep-sea coral evidence for lower Southern Ocean surface nitrate concentrations during the last ice age. PNAS, 114(13). https://doi.org/10.1073/pnas.1615718114